J. Fluid Mech. (1994), vol. 270, pp. 277–296

Quantitative measurements of three-dimensional structures in the wake of a circular cylinder

By HUSSEIN MANSY, PAN-MEI YANG AND DAVID R. WILLIAMS

Mechanical and Aerospace Engineering Department, Illinois Institute of Technology, Chicago, IL 60616, USA

(Received 29 July 1993 and in revised form 7 January 1994)

The fine scale three-dimensional structures usually associated with streamwise vortices in the near wake of a circular cylinder have been studied at Reynolds numbers ranging from 170 to 2200. Spatially continuous velocity measurements along lines parallel to the cylinder axis were obtained with a scanning laser anemometer. To detect the streamwise vortices in the amplitude modulated velocity field, it was necessary to develop a spatial decomposition technique to split the total flow into a primary flow component and a secondary flow component. The primary flow is comprised of the mean flow and Strouhal vortices, while the secondary flow is the result of the three-dimensional streamwise vortices that are the essence of transition to turbulence. The three-dimensional flow amplitude increases in the primary vortex formation region, then saturates shortly after the maximum amplitude in the primary flow is reached. In the near-wake region the wavelength decreases approximately like $Re^{-0.5}$, but increases with downstream distance. A discontinuous increase in wavelength occurs below $Re = 300$ suggesting a fundamental change in the character of the three-dimensional flow. At downstream distances ($x/D = 10$–20), the spanwise wavelength decreases from $1.42D$ to $1.03D$ as the Reynolds number increases from 300 to 1200.

1. Introduction

The flow around right circular cylinders is geometrically one of the simplest cases, but as discussed by Morkovin (1964) it is one of the most perplexing. Because of the fundamental nature of flow around a cylinder, it is of great interest to study the formation and evolution of these structures. Roshko (1954) identified the Reynolds number range of 150 to 300 as the transition range between stable vortex streets and the irregular range. It is in the transition range of Reynolds number where three-dimensional disturbances appear. The three-dimensional vortical structures that develop in flows behind two-dimensional bluff bodies have been reported for decades, yet their origin, structure and the role they play in the transition process from laminar to turbulent flow is not yet clear.

It is recognized that two-dimensional flow simulations do not accurately reflect transition, i.e. transition is inherently a three-dimensional process. Therefore, one must understand the evolution of three-dimensional disturbances in order to be able to predict transition. Three-dimensionalities that arise in the near wake of bluff bodies at low Reynolds number can be classified into three main categories based on their shape and size relative to the cylinder diameter. They may occur as quasi-periodic three dimensionalities with a spanwise wavelength of approximately a cylinder diameter, or

as localized dislocations and turbulent spot-like structures, or as oblique shedding of the Strouhal vortices with long wavelengths greater than 10 cylinder diameters.

Vortex dislocations are an important class of three-dimensionality in the wake. When non-uniform vortex shedding occurs along the axis of the cylinder, then three-dimensional reconnection of vorticity must occur at the interface between cells of vortex shedding. The cellular patterns have been studied on cylinders and tapered cylinders by Gaster (1969, 1971), Papangelou (1992) and Piccirillo & Van Atta (1993). The formation of dislocations in otherwise uniform vortices was studied in shear flows by Browand & Ho (1987). Hammache & Gharib (1989) showed that transition could be delayed by enforcing parallel shedding of the Kármán vortices, thereby reducing the number of dislocations. The generation of small-scale vortical structures at the sites of reconnection lead to turbulent spot-like regions as investigated by Williamson (1992). This mechanism of turbulence generation is localized to the regions of reconnection along the span of the cylinder, which makes it fundamentally different from the spanwise quasi-periodic type of transition. In contrast to dislocations, the small-scale disturbances exist along the entire span of the cylinder above the critical Reynolds number (≈ 170) and appear every cycle of the Strouhal vortices. The dislocation phenomena have been studied in wakes by Gerrard (1966), Gerich & Eckelmann (1982), Eisenlohr & Eckelmann (1989), Williamson (1989), Lewis & Gharib (1992), and Yang, Mansy & Williams (1993). The connection of dislocations with the transition process was established by Williamson (1992).

In the current study attention is focused on investigating some characteristics of the small-scale three-dimensional disturbances, which contribute to turbulence generation and the decay of the primary structures. The majority of studies of three-dimensional wave development have been based on flow visualization. To our knowledge, the first systematic observation of the three-dimensional flow was by Hama (1957). He bled dye through the cylinder surface in a water channel to examine the onset of three-dimensional waves in the Strouhal vortices, and observed the regular occurrence of spanwise waviness of the primary vortices in the wake of a circular cylinder at Reynolds numbers, Re, from 200 to 300. The three-dimensional structures appeared intermittently for Re of 150 to 200 and disappeared as the Re decreased below 150. His flow visualization photographs indicated that the spanwise wavelength of the structures decreased by almost a factor of 3 as the Re was increased from 190 to 313.

Using a hot-wire anemometer Bloor (1964) found that turbulent motion is absent for Re less than 200, and the three-dimensional distortions leading to turbulence in the wake begin to appear around $200 < Re < 400$. The Strouhal vortices become turbulent during their formation process at Reynolds numbers above 400. She detected the occurrence of transition waves, resulting from the separated shear-layer instability for Reynolds numbers greater than 1300.

Gerrard (1978) observed the occurrence of concentrated streamwise vortices which took the form of 'fingers' of dye in his flow visualization studies for Reynolds numbers in the range $140 < Re < 500$. The fingers appeared in the region between vortices of the same sign and crossed the wake centreline. The fingers were randomly distributed along the span, but they followed each other at the same location from cycle to cycle. He concluded that transition to turbulence is primarily due to the three-dimensional distortion of vortices.

The onset of three-dimensionality is not limited to the near-wake region. In the far wake of a circular cylinder, Cimbala, Nagib & Roshko (1988) observed spanwise periodicity at low Reynolds numbers of 140 and 150. Their smoke-wire visualization photographs at $Re = 140$ demonstrated the onset of three-dimensionality beyond 100

cylinder diameters downstream with a spanwise wavelength of around 20 diameters. They suggested that the three-dimensionality was a result of secondary instability based on the interaction of spanwise oblique (and non-uniform) disturbances with the two-dimensional periodic vorticity structures of the far wake.

Meiburg & Lasheras (1988) introduced three-dimensionality into the wake of a flat plate by machining a wavy trailing edge into their model. They found that the resulting secondary disturbances took the form of counter-rotating streamwise vortices with a lambda-shaped structure. The streamwise vortices were located in the braid region formed between consecutive Kármán vortices of opposite signs.

The flow visualization in a circular cylinder near-wake region by Williamson (1988) indicated that there are two different modes of secondary flow associated with different Strouhal frequencies. The first mode (mode A) took the form of vortex loops with a spanwise wavelength of around three cylinder diameters and occurred for Reynolds numbers from 170 to 260. The second mode (mode B) occurred for $Re > 230$ and was associated with the formation of finer-scale streamwise vortices with a spanwise wavelength of around one cylinder diameter at Re of 285. The observed vortex structure and wavelengths were qualitatively consistent with Hama's observations. Williamson (1988) suggested that the Kelvin–Helmholtz instability of the separated shear layers cannot explain the onset of vortex loops or the finer-scale, because secondary vortices associated with this type of instability first begin to form around Re of 1000. The flow visualization studies of Hama (1957) and Williamson (1988) indicated that the spanwise wavelength of the streamwise vortices changed substantially as the Reynolds number increased.

The connection between near- and far-wake three-dimensionality was clearly demonstrated in the quantitative hot-wire measurements by Hammache (1991). He showed that spanwise periodicity may appear in the near wake of a circular cylinder owing to oblique shedding of the primary vortices at low Re, which have the same spanwise wavelength as the three-dimensional structures in the far wake. When this form of secondary flow disturbance is present it leads to earlier transition to turbulence. Williamson & Prasad (1993) used flow visualization to demonstrate a connection between the appearance of three-dimensional patterns in the far wake resulting from the interaction of oblique shedding vortices in the near wake and large-scale two-dimensional waves in the far wake.

Bays-Muchmore & Ahmed (1991) used flow visualization to examine the three-dimensional structure of flow around a cylinder at Reynolds numbers ranging from 330 to 21000. They found streamwise vortices between the primary vortices in the braid region. The mean spanwise spacing did not vary significantly, although the spanwise locations for the vortices was erratic. Interaction between the streamwise vortices and the Strouhal vortices occurred on the upstream facing portion of each Strouhal vortex.

Using direct numerical simulation of the Navier–Stokes equations and assuming a spanwise wavelength of 1.57 cylinder diameters, Karniadakis & Triantafyllou (1992) found that the three-dimensional secondary instability of the two-dimensional vortex street first appears at $Re \approx 200$. The secondary flow resulted in wavy vortex filaments in the near wake that developed a rib-like structure further downstream. They concluded that the wake experiences a period doubling route to transition to turbulence, and found a cascade of period doubling leading to chaotic flow states at $Re = 500$.

From a global instability analysis of the periodic wake to two- and three-dimensional disturbances, Noack, Koenig & Eckelmann (1993) found that the periodic flow is stable with respect to two-dimensional disturbances and is neutrally stable with

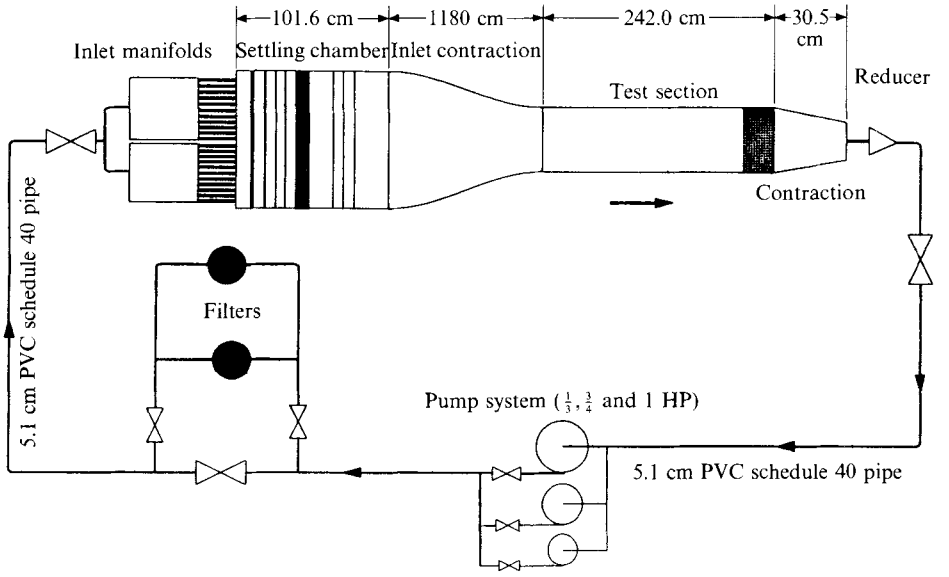

FIGURE 1. Schematic of the water channel.

respect to three-dimensional disturbances at a critical $Re = 170$. They concluded that the most amplified disturbance has a characteristic spanwise wavelength of $1.8D$ for $150 < Re < 200$, where D is the cylinder diameter. However, they also recognized that the quantitative data necessary to confirm the theory is not yet available.

Clearly there is a need for detailed quantitative measurements of the small-scale three-dimensional structures in the cylinder wake. The objective of current work is to obtain a quantitative measure of the spanwise wavelength and strength of the quasi-periodic three-dimensional structures that lead to transition in a circular cylinder wake. In particular, information about the amplitude and wavelength of the initial three-dimensional disturbances and the dependence on Reynolds number is to be examined. Scaling of the wavelength of the small-scale three-dimensional structures with cylinder diameter is to be investigated.

The experimental facility used to acquire the flow velocity information is described in §2. The novel spatial decomposition technique, and the results of the measured spanwise wavelength and strength of the secondary flow are presented in §3, followed by discussion of the results in §4. The conclusions of this study are detailed in §5.

2. Experimental facility

The experiments were conducted at the Fluid Dynamics Research Center in a closed-cycle water channel shown schematically in figure 1. The water channel system was made entirely of stainless steel and plastic to maintain high water quality for extended periods of time. The test section was 20 cm wide, 30 cm high and 180 cm long. The water was filtered to a 30 μm level absolute and polystyrene spheres 2 μm diameter were added as seeding particles for the laser anemometry. Flow speeds in the water channel could be varied from 0.5 cm s^{-1} to 11.5 cm s^{-1}, and were uniform across the test section within 2.5% of the free-stream speed, U_0. The free-stream turbulence level, measured with a hot-film anemometer, was 0.3% of U_0 on average. Five circular cylinders were used during this study with diameters, D, of 0.476, 0.635, 0.953, 1.429 and 1.905 cm, providing a Reynolds number range of 25–2200. Reynolds number is

defined as $U_0 D/\nu$, and ν is the kinematic viscosity. End plates were positioned 24 cm apart for all cylinders giving aspect ratios ranging from 13 to 50. The coordinate system was defined such that the origin was located on the cylinder axis at the mid-span point, the z-axis coincides with the cylinder axis, the x-axis points in the streamwise direction, and the y-axis is in the cross-stream direction.

A forward-scatter scanning laser anemometer (SLA) was used to measure the streamwise component of flow velocity along lines parallel to the cylinder axis. The laser source was a Spectra-Physics model 165 argon ion laser emitting a 514.5 nm wavelength beam. The laser power was kept around 0.15 W during the current tests. The beam was split into two with a Matsushita model EFL-M040B01 acousto-optic modulator. To obtain reversed flow measurements a velocity bias was introduced by shifting one of the beams by 40000 ± 50 kHz with a TSI model 9186A frequency shifter. The light scattered from the seeding particles was collected by a cylindrical lens and imaged onto a TSI model 9162 photomultiplier. The resulting signal was processed with a TSI model 1990C counter-type signal processor. The overall system velocity resolution was 7.6×10^{-3} cm s^{-1}. The 'data ready' signal from the processor triggered a 12-bit A/D board on a MASSCOMP 5500 data acquisition workstation to acquire the processor output signal. Because the data were acquired at random intervals in time and position along the scan, it was necessary to interpolate the raw data to obtain uniformly spaced data. More details of the SLA system can be found in Williams & Economou (1987).

The choice of the scanning rate of the SLA system is a trade-off between spatial and temporal resolution. The scanning rate was high enough that at least 10 scans were obtained for each Strouhal vortex shedding cycle. The scanning rate was chosen to be either 10 or 20 scans s^{-1} depending on the spatial resolution required. The randomly spaced data along each scan were interpolated to get the velocity at 128 equally spaced locations. The post-processing provided quasi-instantaneous velocity profiles along the 4 cm long scanning line. Data rates of the SLA system were kept high enough such that on average, at least two velocity samples were taken at each spatial location. Typical data rates were 5000 points s^{-1} when scanning at 20 scans s^{-1} and 3500 points s^{-1} when scanning at 10 scans s^{-1}.

3. Results

The SLA system yields a time history of the streamwise velocity along the scanning line in the form of a two-dimensional velocity map. Figure 2 shows a typical velocity map obtained for the 0.953 cm diameter cylinder at $x/D = 2.0$, $y/D = 0.5$ and $Re = 600$. The grey levels on the right-hand side of the graph indicate velocity levels which range from -0.36 cm s^{-1} to 6.52 cm s^{-1}. In the map, velocity is displayed as a function of spanwise direction, z, (horizontal axis) and time (vertical axis). Time starts at the top left-hand corner of the figure and continues down the first strip of data. The second strip is a continuation of the first strip and third is a continuation of the second, etc. The scanning length is 4.4 cylinder diameters, and the time corresponding to each strip is 23.2 s. The Strouhal vortices appear as two-dimensional structures of high and low velocity (light and dark) bands nearly parallel to the z-direction. Dislocations in the primary vortices occur owing to the difference in shedding frequencies along cylinder span, which can be seen in the bottom half of the third strip.

The secondary flow associated with streamwise vortices appears as low- and high-velocity patches within the velocity map, and tend to be more visible during the low-velocity part of Strouhal vortex oscillation. The streamwise vortical structures seem to

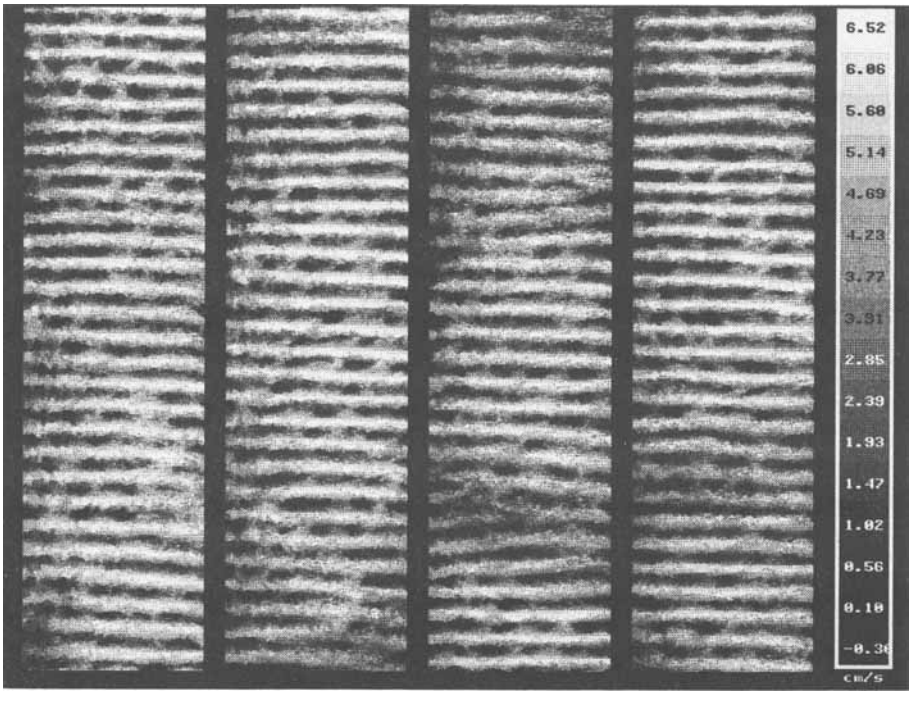

FIGURE 2. The velocity map, $u(z, t)$, obtained at $x/D = 2.0$, $y/D = 0.5$ and $Re = 600$ for the 0.953 cm diameter cylinder. The scanning length is 4.4 cylinder diameters, and the time corresponding to each strip is 23.2 s.

have no preferred spanwise location, i.e. they wander back and forth along the axis of the cylinder. Attempts were made to lock-in the three-dimensionality to a particular spanwise location with small pieces of tape and tubing placed along the cylinder. Although these surface disturbances produced a measurable change in the mean and r.m.s. velocity profiles, they failed to lock-in the three-dimensional structures. The spanwise wandering phenomenon made conditional-averaging techniques virtually useless for resolving the details of the three-dimensional disturbances. Nevertheless, with the SLA system it was possible to obtain the desired measurements of the three-dimensional flow.

3.1. *Velocity decomposition procedure*

In order to extract quantitative information about the secondary flow from the total flow velocity maps, a new technique has been developed to decompose the flow into two components. The first component consists of the mean flow and the primary instability, while the second corresponds to the three-dimensional structures. The very long wavelength (greater than 10 cylinder diameters) three-dimensional disturbances are primarily due to non-parallel vortex shedding (vortex dislocations) and are considered to be part of the primary flow. Everything else becomes the three-dimensional signal.

Typically, the velocity map information consists of 10–20 thousand scans. For each scan, the primary velocity component was calculated, then subtracted from the total velocity to obtain the three-dimensional component. A velocity signal along one scan is shown in figure 3. The velocity profiles of the mean plus primary and the three-dimensional components of the flow have also been plotted.

Under ideal conditions the two-dimensional primary flow would produce a uniform velocity signal along the scan (at fixed x- and y-coordinates), with an amplitude that

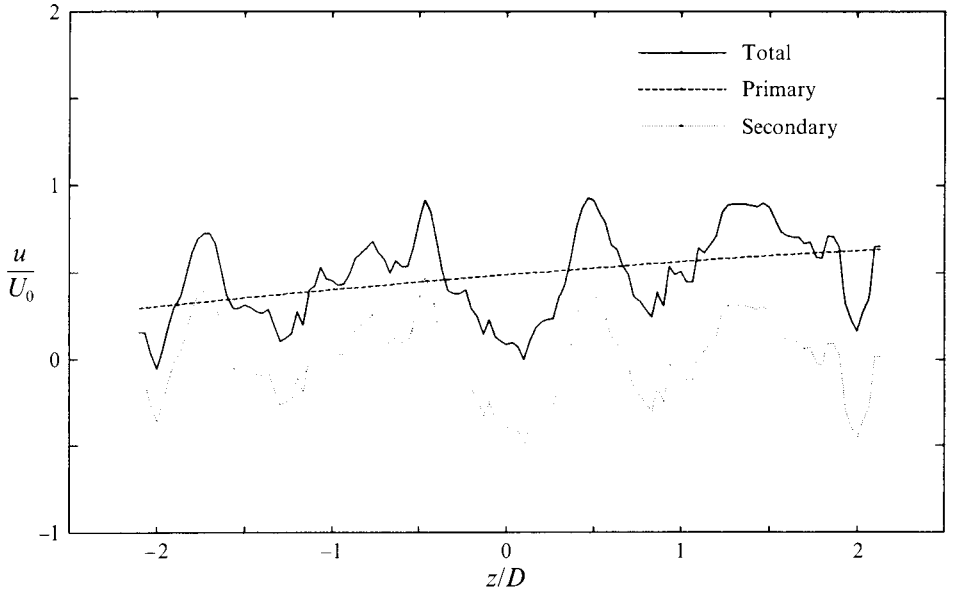

FIGURE 3. The velocity signals of the total, primary and secondary flow components along one scan at $x/D = 2.0$, $y/D = 0.5$ and $Re = 600$.

is modulated at the Strouhal frequency. In that case the average velocity along the scan could serve as an estimate of the two-dimensional flow velocity component magnitude. However, owing to non-parallel shedding, large wavelength three-dimensional effects and the associated vortex dislocations create non-uniformities in the velocity profile along the scan. The otherwise uniform velocity distribution then exhibits slight curvature often with a single minimum or maximum. Therefore, the second-order polynomial in z that best fits the velocity distribution in a least square sense was chosen to represent the primary flow component.

Figures 4(*a*) and 4(*b*) display velocity maps corresponding to the primary and secondary components obtained after decomposition of the total flow shown in figure 2. It is clear from figure 4(*a*) that the vortex shedding is not exactly parallel to the cylinder axis. The phase distribution along the z-axis at the fundamental frequency indicates that the Strouhal vortices are inclined by an average of 20° with respect to the cylinder axis. Although the primary flow contains some spot-like three dimensionality (dislocations), it is free from the small-scale three dimensionality. Here, the dislocations appear as the joining of two low-velocity regions at the left-hand side of the third strip with one low-velocity region at the right.

The secondary flow component, shown in figure 4(*b*), contains three-dimensionality that appears as alternating low- and high-velocity spots in the z-direction. These quasi-organized structures occur periodically in time at the vortex-shedding frequency, but wander in the spanwise direction. Usually, they appear to shift laterally in an organized way, which indicates that some interaction takes place between the structures from one cycle to the next. The appearance of the three dimensionality in figure 4(*b*) suggests that their wavelength varies over a relatively broad range. At some locations in the data one observes consistent lateral shifts with a preferred spanwise wavespeed. The details of this behaviour will be reported in a separate paper.

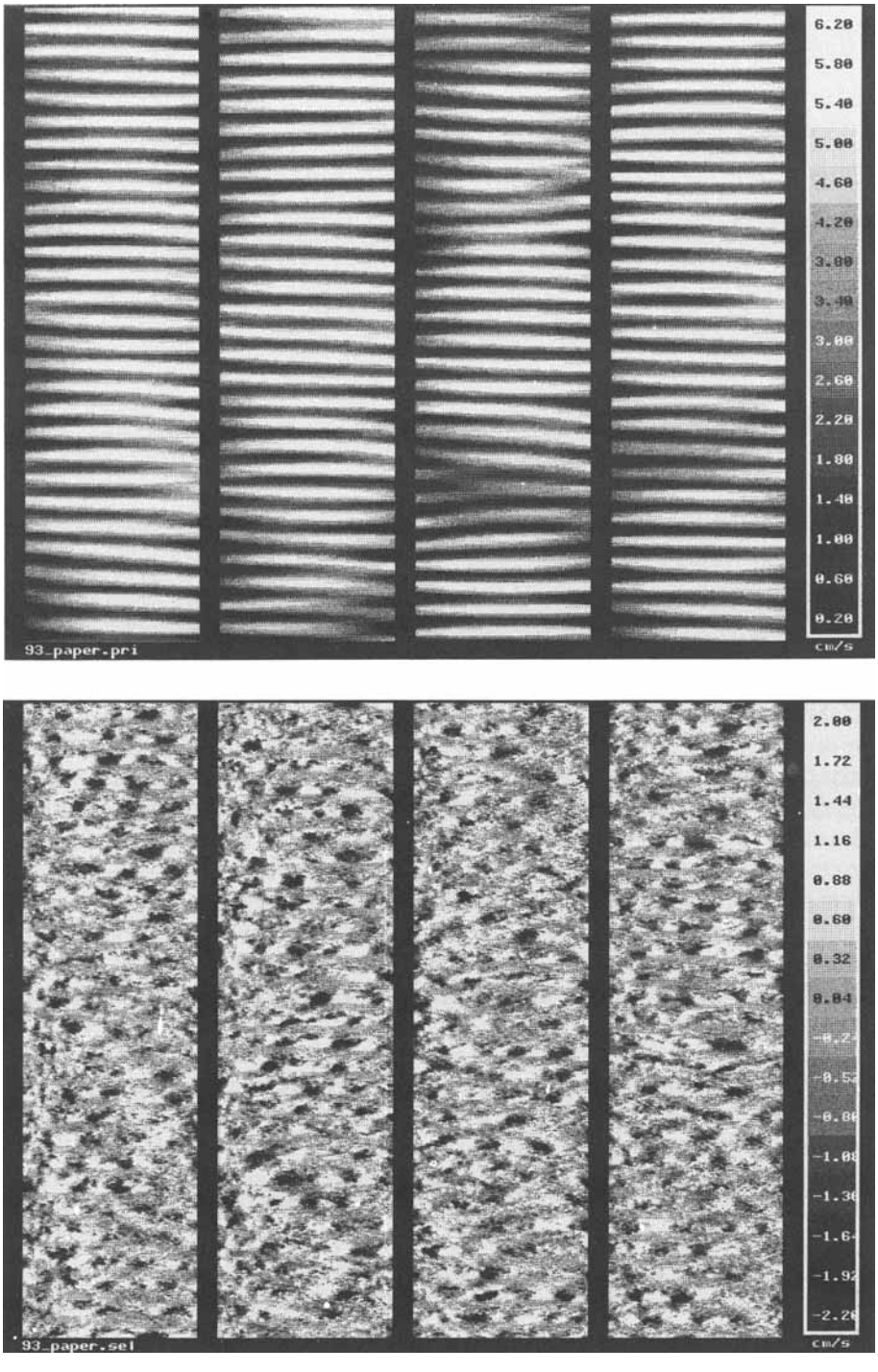

FIGURE 4. (*a*) The velocity map, $u_p(z, t)$, of the primary component extracted from the total flow shown in figure 2 by the spatial decomposition technique. (*b*) The velocity map, $u_{3D}(z, t)$, of the secondary flow component extracted from the total flow signal shown in figure 2.

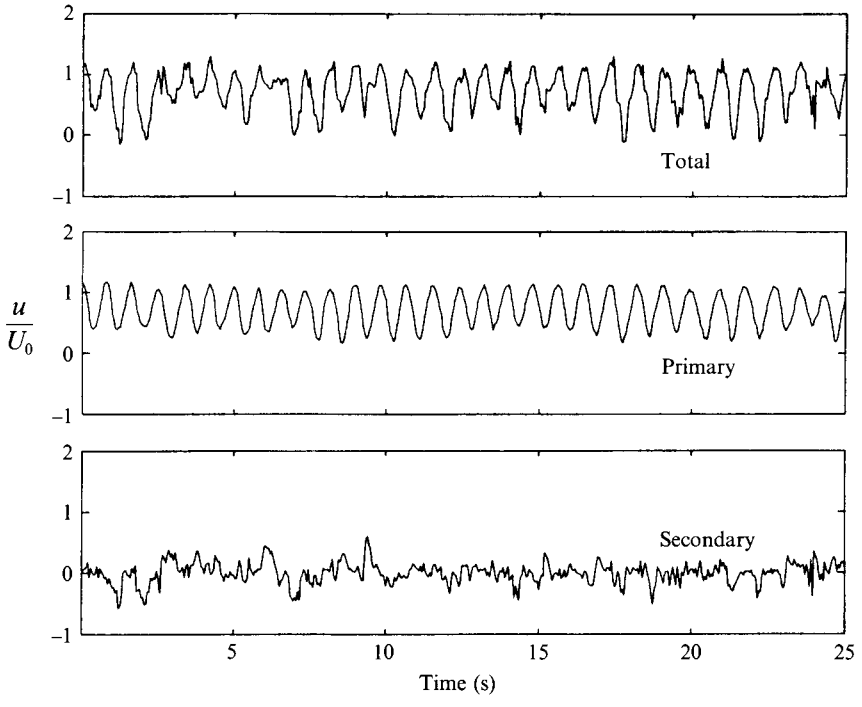

FIGURE 5. Local velocity signals before and after the spatial decomposition at a single point $x/D = 2.0$, $y/D = 0.5$ and $z/D = 0$.

3.2. *Energy estimation of primary and secondary disturbances*

The velocity signal obtained at a single point in the flow ($x/D = 2.0$, $y/D = 0.5$ and $z/D = 0$) is shown in figure 5 before and after the spatial decomposition procedure. The signal was extracted from 25 s of the SLA data along a column in the velocity map, which is equivalent to a signal that would be produced by a single probe. Using signals of this type at each spatial location, the strength of flow oscillations have been calculated as the root mean square, u', of the local velocity after subtracting the local mean. This calculation was applied to the primary and secondary components as well as the total flow.

The velocity traces in figure 5 show that most of the irregularities in the total flow signal are associated with the three-dimensional component, while very little 'noise' appears in the primary component. This confirms the conjectures of Hama (1957) and Bloor (1964) regarding irregularities in hot-wire signals being due to three-dimensional effects. In this experiment the majority of the irregularities in the three-dimensional signal traces are simply a result of the weakly organized, small-scale structures that wander laterally. Careful comparison of the total and primary velocity traces indicates that distortions due to the three dimensionality are generally stronger during the low velocity part of the vortex-shedding cycle.

3.3. *Spatial growth of disturbances*

The spanwise distribution of the r.m.s. velocity of the secondary flow component shown in figure 6 corresponds to the flow shown in figure 4(*b*). It can be seen that the strength of the three dimensional signal amplitude is quite uniform along the cylinder span. Three-dimensional structures occur with practically equal probability at any

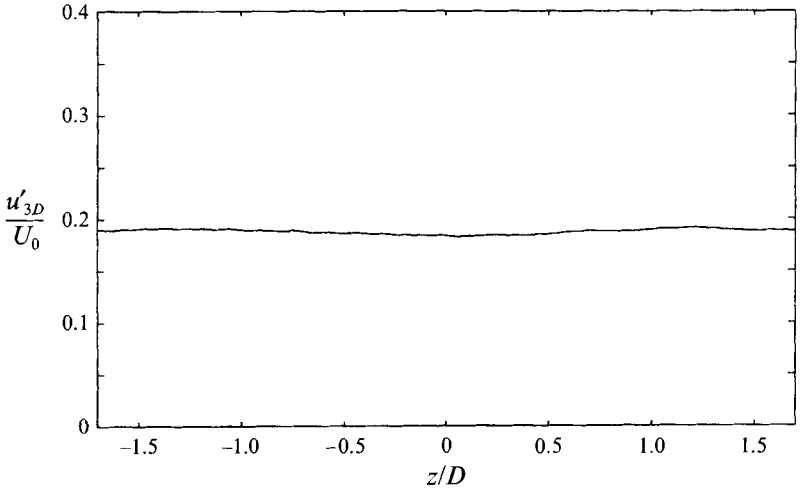

FIGURE 6. Spanwise distribution of the normalized r.m.s. velocity of the three-dimensional component corresponding to flow shown in figure 4(*b*).

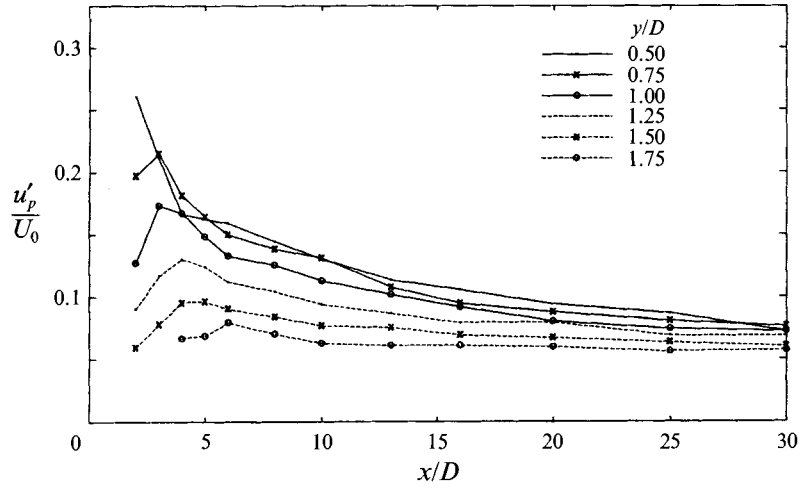

FIGURE 7. The normalized r.m.s. velocity of primary instability, u'_p, at $Re = 600$ for different cross-stream, y/D, and downstream, x/D, stations.

station along the span. Hence, they make an equal contribution to the long-time average of flow quantities along the scan. If the streamwise vortices had been locked-in to a specific location, then one would expect to find peaks and valleys in the r.m.s. distribution.

The primary instability extracts energy from the mean flow as it grows in the streamwise direction until saturation is reached and it begins to decay. This scenario is shown in figure 7 at $Re = 600$ for different cross-stream stations with y/D in the range of 0.5 to 1.75 and for x/D from 2 to 30. As the downstream measurement position was increased, the strength of the primary instability, u'_p, increased to a maximum value followed by slow decay in amplitude. The location of the maximum energy changed from close to $x/D = 2.0$ to $x/D \approx 6.0$ as y/D was increased from 0.5

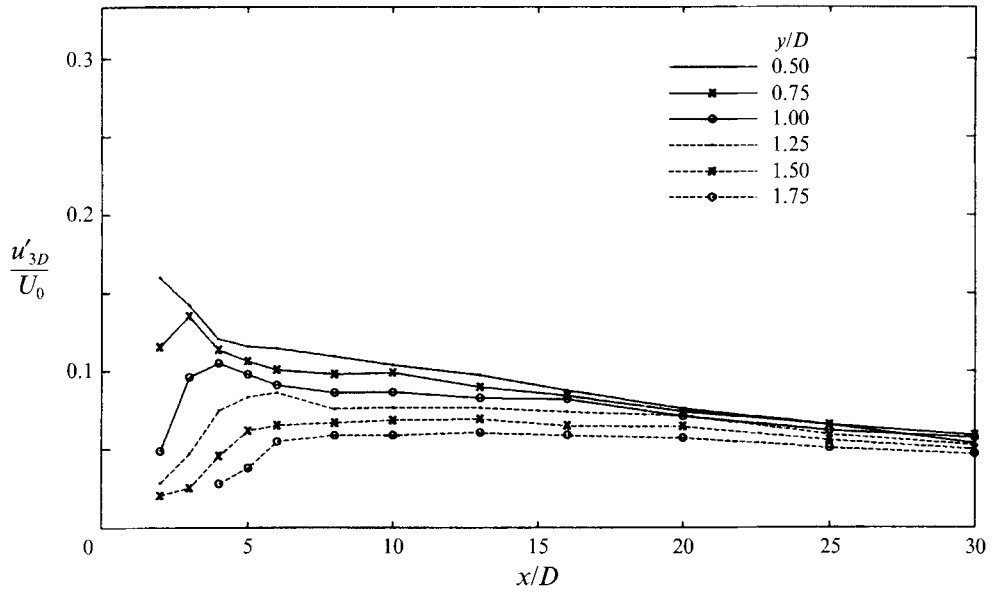

FIGURE 8. The normalized r.m.s. velocity of three-dimensional disturbance, u'_{3D}, at $Re = 600$ for different cross-stream, y/D, and downstream, x/D, stations.

to 1.75. This spatial distribution of the amplitude maxima is in qualitative agreement with the hot-wire measurements of Nishioka & Sato (1978).

The three-dimensional disturbance strength as a function of downstream distance, x/D, is shown in figure 8 at different y/D positions. In general, as x/D increases the three-dimensional component first grows, reaches a maximum and then decays. The strength of the three-dimensionality at $y/D = 0.5$ is higher than that at larger y/D. For the measurement locations shown, the secondary flow is strongest at $x/D = 2$ and $y/D = 0.5$. As y/D increases to 1.75 the maximum in three-dimensional disturbance strength moves to about $x/D = 13$. It is to be noted that the location of the maximum occurs farther downstream than the corresponding maximum of the primary instability. This result is particularly clear for x/D between 3 and 13 and y/D from 1 to 1.75. It is possible that the secondary instability is gaining energy at the expense of the primary instability.

3.4. *Temporal dependence of disturbances*

As seen in figure 5, the amplitude of the three-dimensional disturbance is correlated with the primary instability. To find the phase within the primary oscillation cycle where the three-dimensionality is strongest, the phase difference between the primary and secondary velocity components at the fundamental frequency has been computed. Figure 9(*a*) shows the local spectrum at $x/D = 2.0$, $y/D = 0.5$, and $z/D = 0$. Here, sixteen spectral records have been averaged for each spatial location. The spectra of the total and primary velocity signals exhibit sharp peaks at the Strouhal frequency. The spectrum of the three-dimensional signal over long-time averages is essentially broadband at any point, although occasionally weak peaks can be found at the fundamental Strouhal frequency and/or higher harmonics and subharmonics. The broadband spectra of the three-dimensional component are a result of the spanwise wandering of the small-scale structures.

To get an accurate measure of the phase difference at the Strouhal frequency, the

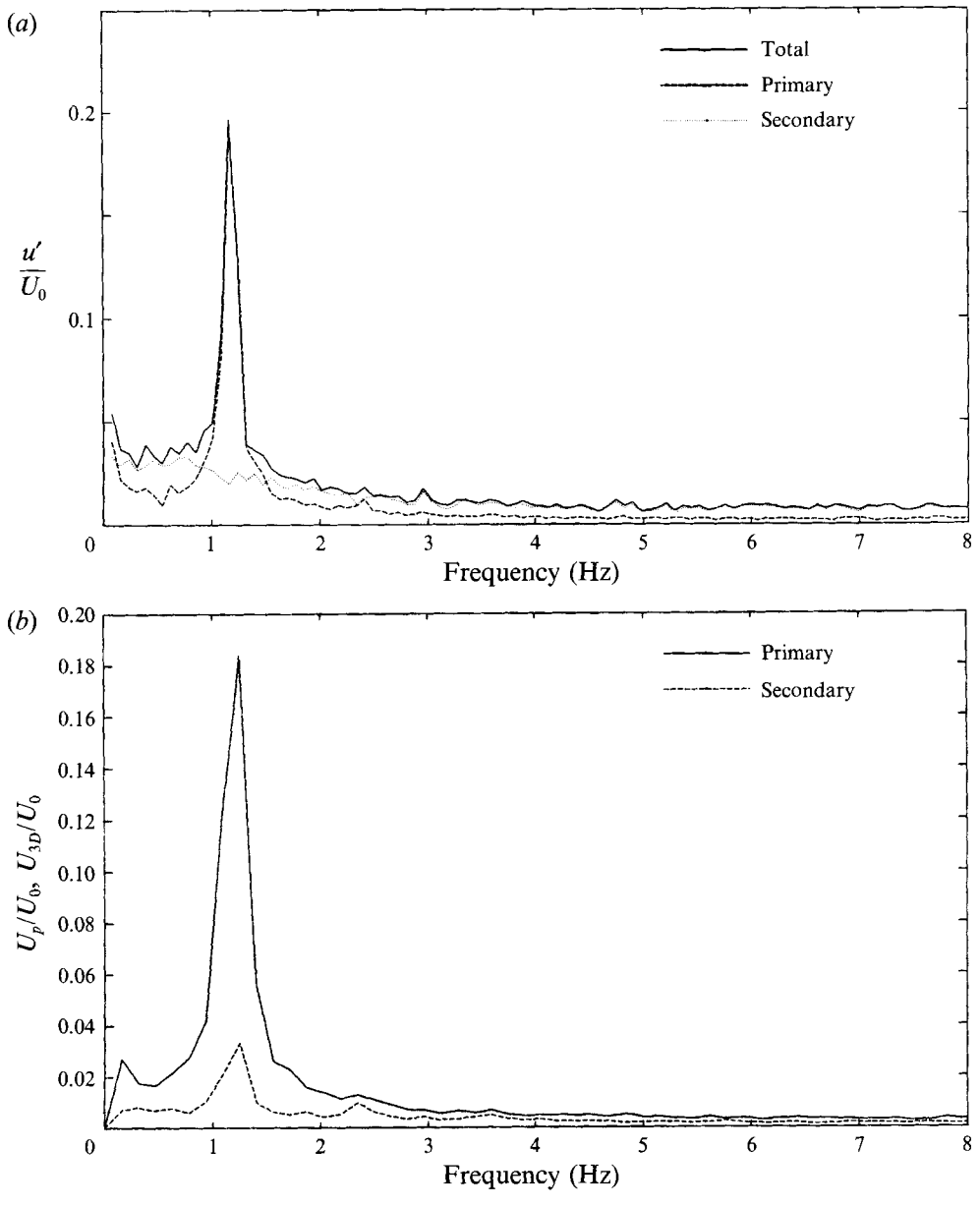

FIGURE 9. (*a*) Spectrum of the total velocity and the primary and secondary velocity components at $x/D = 2.0$, $y/D = 0.5$, $z/D = 1$ and $Re = 600$. (*b*) Spectrum of the space-averaged strength of primary and secondary velocity components at $x/D = 2.0$, $y/D = 0.5$ and $Re = 600$.

average strengths of the primary and three-dimensional structures were defined in terms of spatially averaged signals along each scan. Effectively two new signals were created, one signal representing the strength of the primary flow and the other representing the secondary flow amplitude. For the primary flow, the instantaneous strength was taken as the average in the z-direction of the velocity, i.e.

$$U_p(t) = \frac{1}{L}\int_0^L u_p(z, t)\,\mathrm{d}z.$$

Similarly, the strength of the secondary flow was calculated as the r.m.s. velocity along each scan, i.e.

$$U_{3D}(t) = \left(\frac{1}{L}\int_0^L u_{3D}^2(z,t)\,\mathrm{d}z\right)^{0.5}.$$

Next, the cross-spectra of the $U_p(t)$ and $U_{3D}(t)$ components were computed. The results in figure 9(*b*) show sharp peaks at the Kármán-shedding frequency and smaller peaks at the first harmonic. Since the dominant frequencies in the primary and the secondary flow signals are equal, it can be concluded that the r.m.s. of the three-dimensional signal reaches a maximum only once during the primary oscillation cycle.

The phase difference between the primary and secondary signals at the Strouhal frequency has been calculated for the data set of figure 2. The phase difference was found to be 184°, indicating that the strongest three-dimensional signal occurs during the lowest-velocity part of the primary oscillation cycle. The spatial dependence of the phase difference in the x- and y-directions from $y/D = 0.5$ to $y/D = 1.75$ is shown in figure 10. The phase difference decreases as the scanning location is moved away from the wake centreline. In the downstream direction the phase difference shifts toward 360°, and decreases at larger off-centreline distances. A 360° phase difference means that the strongest three-dimensional signal occurs at the highest-velocity part of the Strouhal oscillation cycle. A decrease in phase indicates that the three-dimensional maximum occurs earlier during the oscillation cycle of the primary instability.

With increasing y/D the maximum in three-dimensional signal strength occurs closer to the peak in the $U_p(t)$ signal. This is consistent with flow visualization studies that showed the three-dimensional disturbances occur in between the primary vortices, particularly in the so-called braid region.

3.5. *Spanwise wavelength measurements*

Earlier wake studies of the small-scale streamwise vortices relied almost exclusively on flow visualization to determine their spanwise wavelength. In the current study, the wavelength was evaluated by calculating spatial autocorrelations. Because noise is usually uncorrelated and contributes to the correlation value primarily at zero shift, it is possible to detect the presence of periodic signals buried in background noise and to calculate their period. The autocorrelation function of periodic signals exhibits spatial periodicity at the same wavenumber as the original signal. Gupta, Laufer & Kaplan (1971) and Lee, Eckelmann & Hanratty (1974) calculated correlation functions to estimate the size of spanwise structures in boundary layers using signals from multiple sensors (10 in the former and 20 in the latter).

In the current study, the autocorrelation function, $R_{uu}(l,t)$, of the streamwise velocity signal, $u(z,t)$ at 128 points in the z-direction, was used to compute the spanwise wavelength of the secondary flow, $\lambda_z(t)$. For records of finite length, the autocorrelation function was calculated as,

$$R_{uu}(l,t) = \frac{\frac{1}{M}\sum_{z=1}^{M} u(z,t)\,u(z-l,t)}{\frac{1}{M}\sum_{z=1}^{M} u^2(z,t)},$$

where M is the number of points per record and l is the spatial shift. As seen from the above equation, the autocorrelation is computed by shifting the signal to obtain $u(z-l,t)$, multiplying it by the unshifted sequence then summing all the values of the

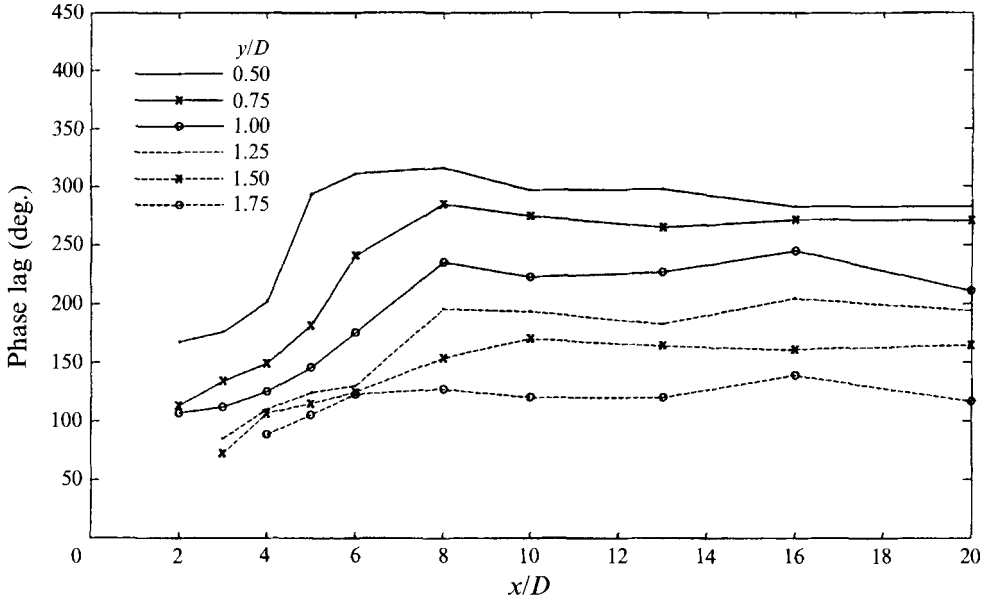

FIGURE 10. Spatial dependence of the phase difference between the primary and the secondary flow components at the Strouhal frequency.

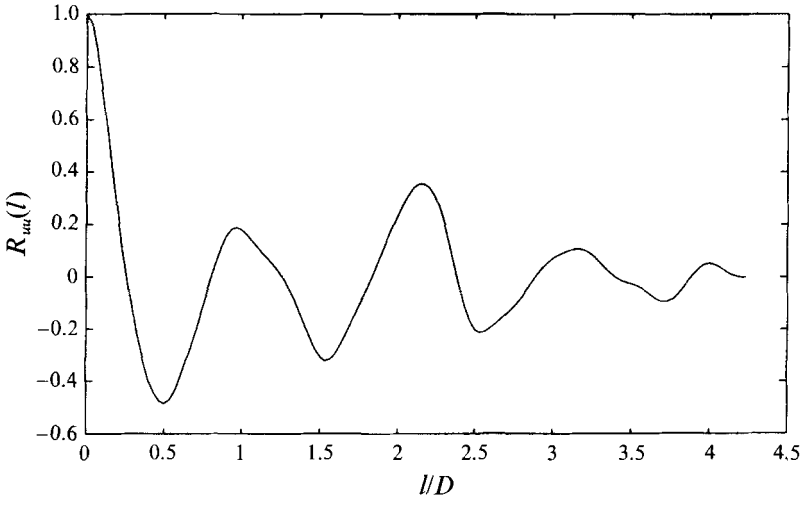

FIGURE 11. The autocorrelation function for decomposed three-dimensional signal displayed in figure 3, $Re = 600$, $x/D = 2.0$, $y/D = 0.5$.

product. $R_{uu}(l, t)$ is normalized by the spatial mean square value of the signal which equals $R_{uu}(0, t)$.

Figure 11 shows the autocorrelation function for the three-dimensional signal displayed in figure 3. The periodicity in the autocorrelation function is apparent, and its period can be found by searching for maxima and minima. As the shift is increased, uncorrelated random noise in the signal makes little contribution to the summation.

Because the measured velocity profiles have a finite length of 128 spatial locations, for correlation calculations, velocity records are assumed to have zero value outside the record length. Therefore, the product $u(z, t)\, u(z-l, t)$, vanishes when the shift is larger

than the data length leading to a finite length correlation. Moreover, for large shifts the number of terms in the summation may be too low to obtain an accurate measure of the location of peaks and valleys in the correlation. To retain high accuracy in calculating the wavelength, shifts with more than three quarters of the record length were avoided, which sets the upper limit on wavelengths that could be detected using this technique.

Since there is a peak in the correlation at the first bin (zero shift), the next minimum in the correlation must occur after or at the second bin and the first peak (the peak with smallest non-zero shift) has to appear at or after the third bin. This sets the lower limit on the smallest measurable wavelength. The 42 mm long scanning length, divided into 128 measurement locations, provides a spatial resolution of 0.3 mm. When the location of the first minimum is used to calculate wavelength, this scanning length corresponds to a detectable wavelength range of 0.6–84 mm, and a preferred working range of 0.6–62 mm with a resolution of 0.6 mm. If the location of the first maximum is used, then the possible range becomes 0.6–42 mm, and the working range is then 0.6–31 mm with a resolution of 0.3 mm.

3.5.1. *Wavelength estimation*

For each scan, i, the calculated autocorrelation function was searched for the first maximum, $l(t)$, which measured the instantaneous wavelength, $\lambda_z(t)$. For comparison purposes, the shift associated with the first minimum was also found, which corresponded to half a wavelength. Because finer resolution can be achieved when using the location of the first maximum for wavelength calculations, it was used in the present study to compute wavelength. The difference in the estimated wavelengths obtained from the two techniques was typically within 0.6 mm.

The instantaneous wavelength, $\lambda_z(t)$, was found to vary from scan to scan, so a large number of scans are needed to get an accurate estimate of the average wavelength. Typically, 10000–20000 scans were used in this study for the wavelength calculations, which corresponds to 1000–2000 Strouhal vortices. The instantaneous wavelength $[\lambda_z(t)]$ was computed for all scans, and the number of times, N_λ, a certain λ_z value appears was calculated. The histogram of the wavelength distribution was constructed by plotting N_λ versus λ_z. An average value and a standard deviation of λ_z were then computed. Figure 12 is one histogram that shows wavelength distribution of the flow shown in figure 4(*b*).

The variation of wavelength in the spanwise direction and in time $\lambda_z(z, t)$ can also be seen in the velocity map of figure 4(*b*). The scanning length covers only four to five structures on average, which does not make it possible to get an accurate measure of the spanwise distribution of $\lambda_z(z)$. However, we believe the variation of $\lambda_z(z)$ may be approximated by the distribution of $\lambda_z(t)$ as seen in the histogram in figure 12. Therefore, figure 12 shows the probability of occurrence of $\lambda_z(t)$. Careful investigation of instantaneous velocity profiles $u(z)$ such as seen in figure 3 shows that the wavelength of individual streamwise vortical structures is not perfectly constant. At any instant there is a range of different wavelengths along the span. Furthermore, it is seen from the velocity maps that the wavelength varies in both z and t. Therefore, the spanwise wavelength measured is the 'most probable' wavelength of the streamwise vortical structures, which are not perfectly periodic.

Noise due to irregularities in the three-dimensional field or to other external causes may give rise to inaccuracies in calculating λ_z. It is important to assess the effect of external noise level on the measured wavelength value. To test this effect, a high signal-to-noise ratio was enforced by choosing scans with relatively strong three-dimensional

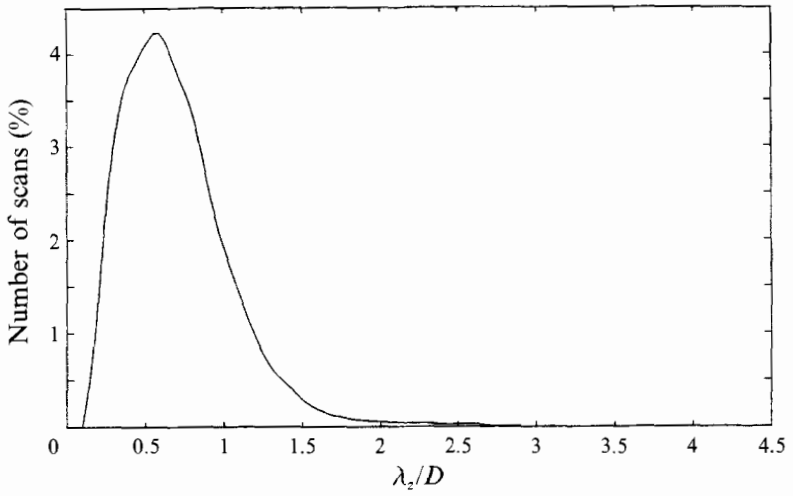

FIGURE 12. A histogram showing the percentage number of scans that correspond to a certain spanwise wavelength, λ_z, for the flow shown in figure 4(*b*), $x/D = 2.0$, $y/D = 0.5$, and $Re = 600$.

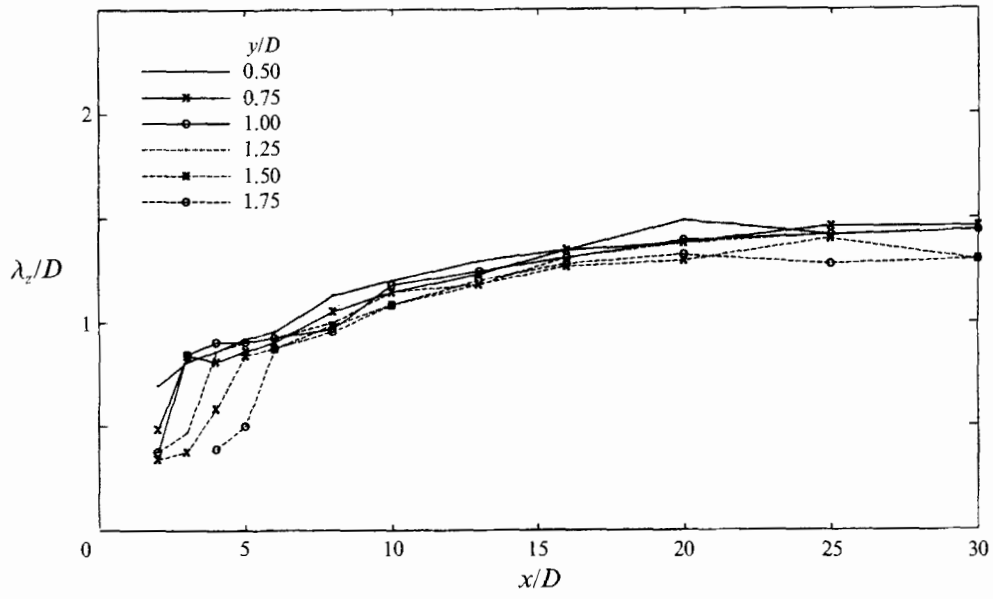

FIGURE 13. Spanwise wavelength, λ_z, dependence on streamwise and cross-stream distance at $Re = 600$.

signal amplitude for λ computations. A threshold was set such that only the strongest 50% of the scans were used for these calculations. For the threshold case, the calculated average wavelength values were about 6–10% higher than the non-threshold results.

3.6. *Spatial dependence of the spanwise wavelength*

Measurements indicate that the spanwise wavelength of the three-dimensional disturbances depends on both the streamwise and cross-stream directions. Results are plotted in figure 13 at $Re = 600$ for x/D from 2 to 30 and y/D from 0.5 to 1.75. The sensitivity to the streamwise location is clear, particularly for x/D less than 6. The

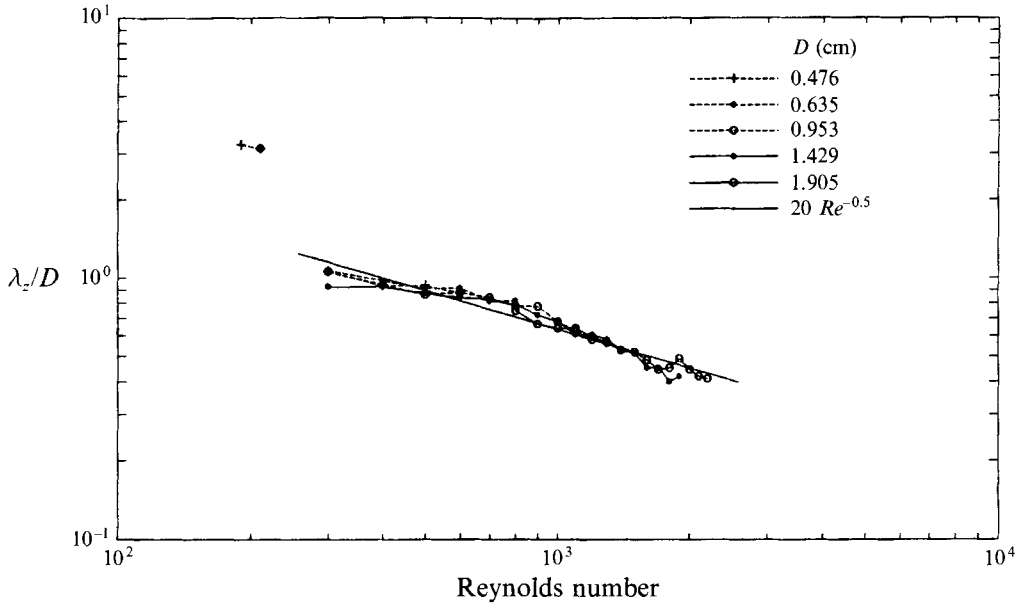

FIGURE 14. Reynolds number dependence of λ_z at $x/D = 3$ and $y/D = 0.5$ for five different cylinders.

spanwise wavelength increases continuously with downstream distance until it reaches an asymptotic value ($\lambda = 1.3$–1.4 diameters) at $x/D = 15$–30. This result suggests that as the downstream distance increases, smaller structures decay while larger ones are amplified. The wavelength is not as sensitive to cross-stream location. As y/D increases from 0.5 to 1.75 slightly smaller wavelengths are detected. It should be noted that the continuous change in wavelength does not rule out the possibility of pairing of structures, since the λ_z values plotted here are long-time averages. The range of instantaneous wavelength, $\lambda_z(t)$, that occurs at any spatial location is very wide, and covers almost all the data range in the figure. The plotted λ_z value is the average wavelength.

3.7. *Secondary flow dependence on Reynolds number and cylinder diameter*

The effect of Reynolds number and cylinder diameter on λ_z was studied by varying both the free-stream speed and cylinder diameter. Five different diameter cylinders were used for this experiment. The scanning location was fixed at $x/D = 3.0$ and $y/D = 0.5$, and the Reynolds number was varied from 70 to 2200. For Reynolds numbers below 160, the secondary flow was not detected. For Reynolds numbers in the range 160–180, the appearance of the streamwise vortices was intermittent. Above an Re of 180 the streamwise vortices appeared regularly during each cycle of primary flow oscillation.

The measured wavelength at $x/D = 3$ for all five cylinders is plotted against Reynolds number in figure 14, which illustrates the dependence of the λ_z on Reynolds number. At a Reynolds number of 300, λ_z is about 1.0 diameter. As the Reynolds number increases the wavelength decreases continuously to 0.39 diameters at a Reynolds number of 2200. The normalized wavelength λ/D was found to scale approximately with $Re^{-0.5}$. Perhaps coincidentally a similar dependence of the Bloor–Gerrard vortices at higher Reynolds number was found by Wei & Smith (1986). The continuously decreasing wavelength suggests that there is no fundamental change

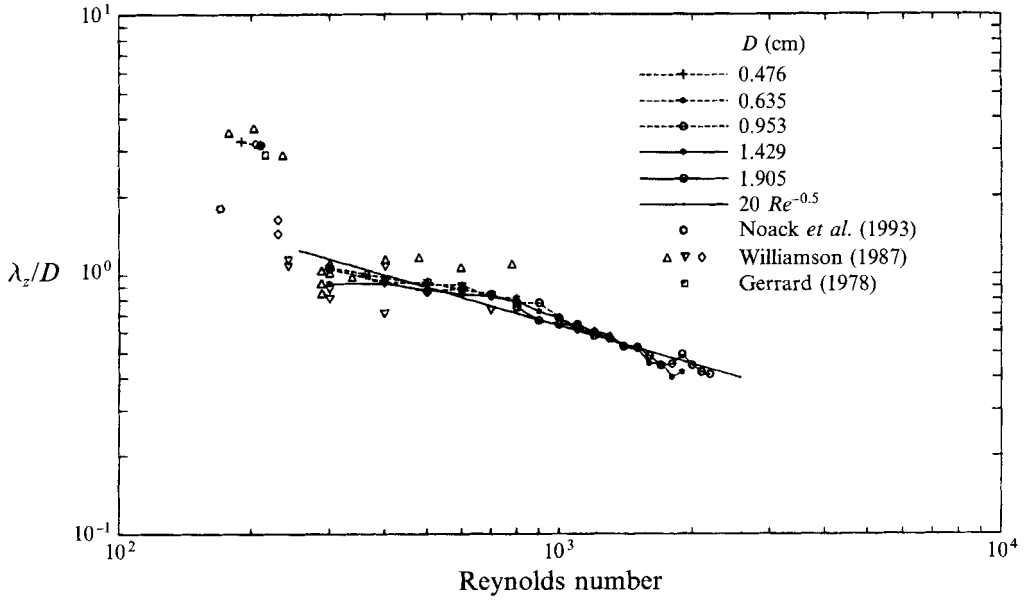

FIGURE 15. Comparison of the λ_z data from figure 14 with the flow visualization by Williamson (1987), Gerrard (1978), and the prediction by Noack *et al.* (1993).

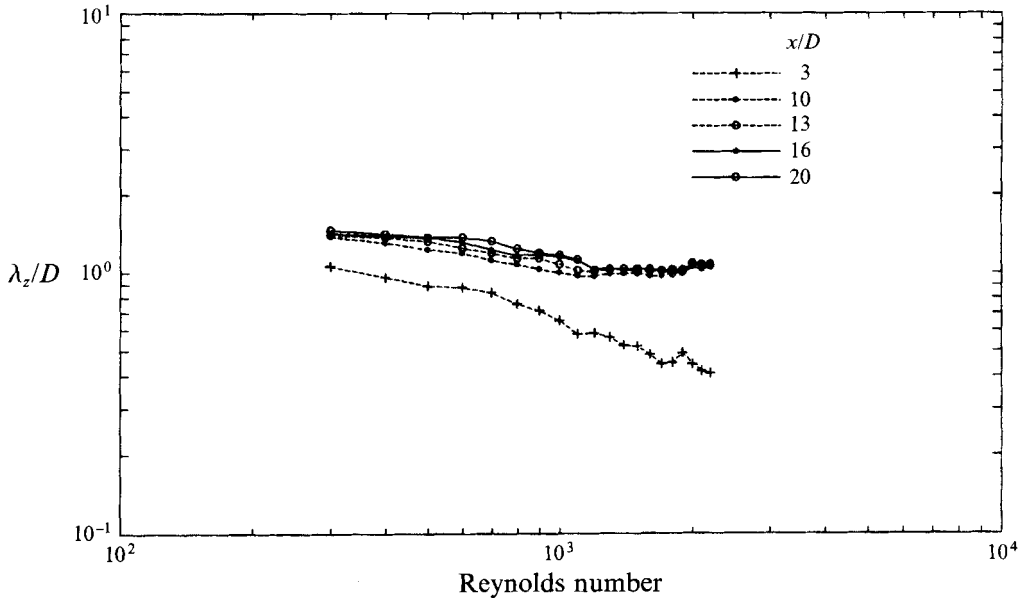

FIGURE 16. Downstream dependence of spanwise wavelength, λ_z, for Re = 300–2200 and x/D = 3–20.

in the origin or nature of the secondary flow under investigation. However, a discontinuous increase in wavelength occurs when the Reynolds number decreases from 300 to 200. At Re = 200 the wavelength was 3.2 diameters, suggesting a change in the character of secondary flow. These large values of λ_z are consistent with Williamson's (1987) observations. Flow visualization results from Williamson (1987)

and Gerrard (1978), along with the wavelength calculated from global stability analysis of the periodic flow (Noack *et al.* 1993), have been superposed on the present set of measurements in figure 15. Noack *et al.* found the characteristic wavelength was 1.8 diameters at a critical Reynolds number of 170. When the measured wavelength of the smaller scale three-dimensionality in the current study is extrapolated to $Re = 170$ using the 20 $Re^{-0.5}$ dependence, an extrapolated value of $\lambda_z = 1.53D$ is found.

Figure 16 shows wavelength measurements for x/D in the range of 10–20. The spanwise wavelength decreases from $1.42D$ to $1.03D$ as the Reynolds number increases from 300 to 1200. A very small change in wavelength occurs for $Re = 1200$–2200 and $x/D = 10$–20.

5. Conclusions

Quantitative measurements with a scanning laser anemometer have provided new insight into the structure of the small-scale, three-dimensional disturbances in the near-wake region. A spatial decomposition technique was developed to extract the three-dimensional component from the total velocity map signal. The three-dimensional structures found in the near wake are strongest close to the cylinder during the formation of the primary vortices. They appear intermittently for Reynolds number in the range of 160–180 and regularly above 180–200. The amplitude of the three-dimensional signal is tied with the primary instability oscillation cycle. Some coupling between structures that occur at one cycle and those at the following cycle exists, but the three-dimensional structures wander in the spanwise direction in a weakly organized fashion. The spanwise wandering is responsible for much of the irregularity seen in single-point velocity signals obtained by previous investigators. At certain regions in the wake it appears the secondary flow gains energy at the expense of the primary instability. The wake supports a wide range of spanwise wavelengths. As the wake develops downstream the larger scales are amplified and smaller scales are attenuated. The average wavelength increases with downstream distance, but is not very sensitive to cross-stream distance.

It has been conclusively shown that the spanwise wavelength decreases continuously like $Re^{-0.5}$ as the Reynolds number increases from 300 to 2200. A discontinuous increase in wavelength takes place as Re decreases from 300 to 200 suggesting a fundamental change in the character of the secondary flow.

We gratefully acknowledge the support of The Office of Naval Research under Grant no. 00014-90-1420, monitored by Dr Edwin Rood.

REFERENCES

BAYS-MUCHMORE, B. & AHMED, A. 1991 On the streamwise vortices in the immediate wakes of circular cylinders. *Bull. Am. Phys. Soc.* **36**, 2620.

BLOOR, M. S. 1964 The transition to turbulence in the wake of a circular cylinder. *J. Fluid Mech.* **19**, 290–304.

BROWAND, F. K. & HO, C. M. 1987 Forced, unbounded shear flows. *Nucl. Phys.* B (*suppl.*) **2**, 139.

CIMBALA, J. M., NAGIB, H. M. & ROSHKO, A. 1988 Large structure in the far wakes of two-dimensional bluff bodies. *J. Fluid Mech.* **190**, 265–298.

EISENLOHR, H. & ECKELMANN, H. 1989 Vortex splitting and its consequences in the vortex street wake of cylinders at low Reynolds number. *Phys. Fluids* A **1**, 189–192.

GASTER, M. 1969 Vortex shedding from slender cones at low Reynolds numbers. *J. Fluid Mech.* **38**, 565–576.

GASTER, M. 1971 Vortex shedding from circular cylinders at low Reynolds numbers. *J. Fluid Mech.* **46**, 749–756.

GERICH, D. & ECKELMANN, H. 1982 Influence of end plates and free ends on the shedding frequency of circular cylinders. *J. Fluid Mech.* **122**, 109–121.

GERRARD, J. H. 1966 The three-dimensional structure of the wake of a circular cylinder. *J. Fluid Mech.* **25**, 143–164.

GERRARD, J. H. 1978 The wakes of cylindrical bluff bodies at low Reynolds number. *Phil. Trans. R. Soc. Lond.* A **288**, 351–382.

GUPTA, A. K., LAUFER, J. & KAPLAN, R. E. 1971 Spatial structure in the viscous sublayer. *J. Fluid Mech.* **50**, 493–512.

HAMA, F. R. 1957 Three dimensional vortex pattern behind a circular cylinder. *J. Aero. Sci.* **24**, 156–157.

HAMMACHE, M. 1991 On the evolution of three-dimensionality in parallel and oblique vortex streets. *Bull. Am. Phys. Soc.* **36**, 2701.

HAMMACHE, M. & GHARIB, M. 1989 A novel method to promote parallel vortex shedding in the wake of a circular cylinder. *Phys. Fluids* A **1**, 1611–1614.

KARNIADAKIS, G. E. & TRIANTAFYLLOU, G. S. 1992 Three-dimensional dynamics and transition to turbulence in the wake of bluff objects. *J. Fluid Mech.* **238**, 1–30.

LEE, M. K., ECKELMANN, L. D. & HANRATTY, T. J. 1974 Identification of turbulent wall eddies through the phase relation of the components of the fluctuating velocity gradient. *J. Fluid Mech.* **66**, 17–33.

LEWIS, C. G. & GHARIB, M. 1992 An exploration of the wake three dimensionalities caused by a local discontinuity in cylinder diameter. *Phys. Fluids* A **4**, 104–117.

MEIBURG, E. & LASHERAS, J. C. 1988 Experimental and numerical investigation of the three-dimensional transition in plane wakes. *J. Fluid Mech.* **190**, 1–37.

MORKOVIN, M. 1964 Flow around circular cylinder – a kaleidoscope of challenging fluid phenomena. *Symposium on Fully Separated Flows*, pp. 102–118. ASME.

NISHIOKA, M. & SATO, H. 1978 Mechanism of determination of the shedding frequency of vortices behind a cylinder at low Reynolds numbers. *J. Fluid Mech.* **89**, 61–78.

NOACK, B., KOENIG, M. & ECKELMANN, H. 1993 Three-dimensional stability analysis of the periodic flow around a circular cylinder. *Phys. Fluids* A **5**, 1279–1281.

PAPANGELOU, A. 1992 Vortex shedding from slender cones at low Reynolds numbers. *J. Fluid Mech.* **242**, 299–321.

PICCIRILLO, P. S. & VAN ATTA, C. W. 1993 An experimental study of vortex shedding behind linearly tapered cylinders at low Reynolds number. *J. Fluid Mech.* **246**, 163–195.

ROSHKO, A. 1954 On the development of turbulent wakes from vortex streets. *NACA Rep.* **1191**, 1–23.

WEI, T. & SMITH, C. R. 1986 Secondary vortices in the wake of circular cylinders. *J. Fluid Mech.* **169**, 513–533.

WILLIAMS, D. R. & ECONOMOU, M. 1987 Scanning laser anemometer of forced cylinder wake. *Phys. Fluids* **30**, 2283–2285.

WILLIAMSON, C. H. K. 1987 Three-dimensional transition in the near wake of a cylinder. *Bull. Am. Phys. Soc.* **32**, 2098.

WILLIAMSON, C. H. K. 1988 The existence of two stages in the interaction to three-dimensionality of a cylinder wake. *Phys. Fluids* **31**, 3165–3168.

WILLIAMSON, C. H. K. 1989 Oblique and parallel modes of vortex shedding in the wake of a circular cylinder at low Reynolds numbers. *J. Fluid Mech.* **206**, 579.

WILLIAMSON, C. H. K. 1992 The natural and forced formation of spot-like vortex dislocations in the transition of a wake. *J. Fluid Mech.* **243**, 393–441.

WILLIAMSON, C. H. K. & PRASAD, A. 1993 Wave interactions in the far wake of a body. *Phys. Fluids* A **5**, 1854–1856.

YANG, P., MANSY, H. & WILLIAMS, D. R. 1993 Oblique and parallel wave interaction in the near wake of a circular cylinder. *Phys. Fluids* A **5**, 1657–1660.